Digital Image Correlation Analysis of the Deformation Behavior of Pb-free Solders at Intermediate Strain Rates*

K.E. Yazzie, J.J. Williams, D. Kingsbury, P. Peralta, H. Jiang, and N. Chawla

Digital image correlation (DIC) is a powerful tool for quantifying local stresses and strains. The demand for environmentally benign Pb-free solders and the push toward smaller portable electronics will make it more likely for solder interconnects to encounter mechanical shock through dropping or mishandling. Thus, quantifying the strain rate behavior of Pb-free solders from the quasi-static to the shock regime is essential for developing reliable numerical models of the mechanical shock behavior. In this paper we report on the use of DIC to measure the local strain and strain rate occurring in the neck of Sn-3.5Ag-0.7Cu specimens, at the onset of necking. Tensile tests were conducted in the range $10^{-3}s^{-1}$ – 30 s^{-1}. A parametric study was conducted to identify the optimum DIC parameters for the experimental setup. The effect of microstructure, and applied strain rate on the local values of strain and strain rate is discussed.

INTRODUCTION

The drive to produce environmentally-benign electronic packages has generated great interest in Pb-free alloys.[1–6] The push toward smaller electronic packages for portable electronics has it made it more likely that solder joints may fail by mishandling, such as dropping during manufacture, shipping, or use. The microstructure, creep, and thermal fatigue behavior of Pb-free solders is well understood.[7–9] However, a fundamental understanding of the behavior of Pb-free solders under mechanical shock conditions is lacking. Experimental stress-strain data over a range of strain rates is needed for a fundamental understanding of mechanical shock, as well as for inputs in reliability models. A variety of experimental techniques have been developed to characterize the strain-rate-dependent behavior of materials.[10] Creep and stress relaxation behavior can be quantified using screw-driven machines at very low strain rates. Plate impact tests can quantify material behavior at the high end or impact regime. The strain rates experienced by solders during mechanical shock, e.g. dropping a cell phone or laptop, are in an intermediate range between the quasi-static and dynamic regimes. A precise range of strain rate for these applications has not yet been established. A variety of studies have shown that the range lies somewhere between 10^{-1} s^{-1} and 10^{2} s^{-1}.[11–17] Boyce and Crenshaw[18] have demonstrated that controlled strain rates of up to 500 s^{-1} can be obtained using servohydraulic methods. In a previous study, we have demonstrated the feasibility of mechanical shock loading of bulk pure Sn solder using a servohydraulic load frame.[19]

A fundamental understanding of deformation behavior in these materials, at intermediate strain ranges, requires an accurate means of measuring local strains and strain rates. In addition, numerical modeling requires accurate and reliable inputs of local strain distributions. Local strain and strain rate at necking can be used as constitutive inputs for finite element method (FEM) models. Digital image correlation (DIC) is a state-of-the-art technique for computing full-field displacements, strains, and strain rates on a sample surface.[20–25] Interferometry techniques are also capable of measuring full field surface strains, but the use of gratings or lasers make those techniques time consuming.[26,27] Alternatively, DIC only requires a high contrast, high density speckle pattern applied to the sample surface. A high speed digital camera is typically used to capture the evolution of deformation. DIC makes use of a correlation algorithm to compare successive images of the deforming speckle pattern. The algorithms used compute a displacement field based on local correlation of the positions of individual speckles. The basic principle of DIC is illustrated in Figure 1a. A point with intensity x is deformed by a displacement field u to a final state x′. The

How would you…

…describe the overall significance of this paper?

This paper describes a unique and effective means of quantifying local strains, by high speed imaging and digital image correlation, during intermediate strain rate behavior of Pb-free solder alloys.

…describe this work to a materials science and engineering professional with no experience in your technical specialty?

High speed imaging coupled with digital image correlation provides a unique means of quantifying the local strains and stresses during deformation. This technique is applied to the deformation and necking behavior of Sn-based alloys used in electronic packaging.

…describe this work to a layperson?

Environmentally-benign Pb-free solder alloys are being used in electronic packaging. These new alloys have lower mechanical shock and drop resistance. This research aims at understanding the local mechanisms for failure of these Sn-based alloys under intermediate strain-rate conditions, often encountered in service.

problem of two-dimensional DIC is to solve for u, where the reference and deformed images are related formally by the following equation:[22]

$$x_i' = x_i + u_i + \frac{\partial u_i(x)}{\partial x_j} dx_j \; i, j = 1,2 \quad (1)$$

Where $\partial u_i / \partial x_j$ are the strain components (four strains and two displacements). The quality of DIC depends on the camera resolution, time steps between images, lighting, quality and size of features in the speckle pattern, and correlation parameters.[21,28–31] The most important correlation parameters are the dimension of the zone (facet), *l*, over which the correlation between the reference image and the deformed image is locally applied; and the center-to-center distance between facets, δ. *l* and δ effectively define a virtual strain mesh which deforms with the stochastic pattern, as shown schematically in Figure 1b.

DIC has been used to study the local stresses, strains, and strain rate distribution in metallic alloys,[32–38] composites,[39,40] and biomaterials.[41,42] In the microelectronics field DIC has been used to study the strains of solder interconnects under thermomechanical loading,[43–47] drop testing of electronic boards,[48] and mechanical characterization of underfills.[49] To date, DIC has not yet been used to study the local strain and strain rates at intermediate strain rates in Sn-based alloys. In this study the mechanical behavior of Sn-3.5Ag-0.7Cu (SAC) solder was systematically quantified at strain-rates of $10^{-3}s^{-1}$ – 30 s^{-1}. Local values of strain and strain rate were measured at the onset of necking, in the necking region of the tensile specimen, using DIC. The first part of the paper describes microstructural characterization and experimental results of tensile tests. The second part discusses results of DIC measurements.

See the sidebar for details materials and experimental procedures.

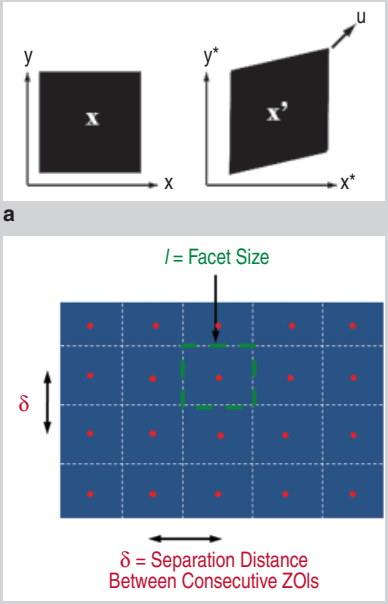

Figure 1. (a) Principle of digital image correlation. A gray scale image **x** is deformed by a displacement field **u** to the state **x′**. The principle of DIC relies on solving for **u**. (b) Virtual mesh defined by the region of interest length, *l*, and center-to-center grid spacing, δ. In this schematic *l* = δ, and the facets touch, but do not overlap. When *l* < δ the facets do not overlap and the ability of DIC to correlate displacements between consecutive images is diminished. When *l* > δ the facets overlap and DIC can better correlate displacements since the overlap produces some redundancy in the local correlations of neighboring facets. (c) Experimental setup for capturing high speed video of tensile tests. (d) Image of a tensile specimen coated with a speckle pattern.

RESULTS AND DISCUSSION

Tensile Behavior and Fractographic Analysis

The microstructures of as-cast SAC alloys after water quenching and fur-

MATERIALS AND EXPERIMENTAL PROCEDURE

Sn-3.5Ag-0.7Cu (Indium Corporation, Ithaca, NY, USA) ingots were used in this study. The ingots were reflowed in a graphite coated aluminum mold with dimensions: 10.5 cm long, 1 cm wide, and 0.8 cm high. A thermocouple placed at the bottom of the solder was used to measure the cooling rate. The samples were heated to 20°C above the melting point (240°C), held for 20 s, and cooled. Fine and coarse microstructures were obtained with a water quench cooling rate of 16.5°C/s and a furnace cooling rate of 1°C/s, respectively. Microstructural characterization was conducted after reflow and cooling. The samples were polished to a final finish with a 0.05 μm colloidal silica solution. Scanning electron microscopy (SEM) was used to characterize the microstructure. Tensile specimens were machined from a section near the bottom of the reflowed blank, where the cooling rate was measured. Microstructure characterization of the tensile specimens prior to testing revealed a uniform microstructure throughout the specimens. The tensile specimens had a 10 mm gage length. A detailed schematic is available elsewhere.[19]

The speckle pattern was applied to the specimen surface as follows. The specimen surface was gently abraded with 600 grit SiC to create a uniform roughness and then rinsed with acetone to remove surface contaminants. The surface was coated with a thin layer of white matte-finish spray paint. Black matte-finish spray paint was sprayed on the white base coat to create a stochastic pattern of speckles on the order of 200 μm wide, or about 4 pixels × 4 pixels in area. White light sources were used to indirectly light the specimen during testing. The test setup is shown in Figure 1c with a typical image of a specimen photographed under these conditions shown in Figure 1d. The servohydraulic grips in this study were highly reflective. The highly reflective surface diminished the ability of the DIC software to accurately compute displacements. To remedy this, the grips were wrapped in white tissue paper, which effectively eliminated reflections.

Tensile tests were performed on a servohydraulic load frame, in displacement control, at nominal strain rates ranging from 10^{-3} s^{-1} to 30 s^{-1}. A high-speed camera (Phantom, Vision Research, Wayne, NJ) was used to record video of the tensile tests using frame rates up to 4,200 frames per second (fps). The recorded video was then converted to 8-bit tiff images. The strain produced in the specimen during the tensile test was analyzed by importing the 8-bit tiffs into commercially available digital image correlation software (ARAMIS, Trillion Quality System, Plymouth Meeting, PA, USA).

nace cooling are shown in Figure 2. The furnace cooled SAC microstructure consisted of Ag_3Sn needles and Cu_6Sn_5 intermetallic several micrometers in size, as shown in Figure 2a. The water quenched SAC microstructure consisted of Sn-rich dendrites and a eutectic mixture of Sn, Cu_6Sn_5, and Ag_3Sn, as shown in Figure 2b. The engineering stress-strain curves for tensile tests of furnace cooled and water quenched Sn-3.5Ag-0.7Cu are shown in Figure 3a and b, respectively. At the highest strain rates an oscillatory wave, caused by reflected elastic waves, was superimposed on the stress-strain curves. In general, all specimens showed an increase in ultimate tensile strength (UTS) with increasing strain rate. For a given strain rate, the water quenched specimens had greater UTS values than the furnace cooled specimens. This is expected since the finer microstructure, particularly in the form of a fine dispersion of Ag_3Sn particles, increases the number of obstacles for dislocation motion. Water quenched specimens had greater strain-to-failure than furnace cooled specimens. This behavior is somewhat unexpected since the coarser microstructures in the furnace cooled specimens would appear to result in lower yield stress and higher ductility. Fractography was performed on the fracture surfaces at the highest and lowest strain rate using SEM. Ag_3Sn needles and Cu_6Sn_5 particles were identified using energy dispersive spectroscopy (EDS) spot scans. The fractography revealed that in the furnace cooled specimens the Ag_3Sn needles fractured extensively and nucleated large voids that reduced the ductility of the furnace cooled specimens, as shown in Figure 4a. The Cu_6Sn_5 particles were rarely found at the bottom of ductile dimples. At the higher strain rate the Ag_3Sn needles were fractured, as shown in Figure 4b. The high triaxial stresses surrounding the Ag_3Sn needles at high strain rate caused them to fracture and nucleate voids. The fracture surface of the water quenched samples consisted of small ductile dimples, most likely nucleated by the fine intermetallic Ag_3Sn and Cu_6Sn_5 particles or in the pure Sn regions, as shown in Figure 5a. The ductile dimples were more numerous in the specimen tested at the highest strain rate, as shown in Figure 5b, due to the enhanced degree of stress triaxiality at the higher strain rate. Thus, the elongated nature of the Ag_3Sn needles appears to be responsible for nucleation of larger voids that could coalesce more easily, and resulted in lower ductility.

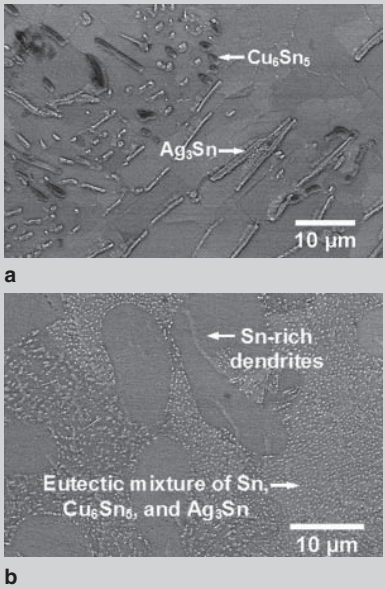

Figure 2. (a) Microstructure of furnace cooled Sn-3.5Ag-0.7Cu. Large Ag_3Sn needles and blocky Cu_6Sn_5 particles exist in a Sn matrix. (b) Microstructure of water quenched Sn-3.5Ag-0.7Cu. Sn-rich dendrites are surrounded by a eutectic mixture of Sn, Ag_3Sn, and Cu_6Sn_5.

Digital Image Correlation Analysis

When conducting DIC analysis, it is important to minimize any potential artifacts that may arise. These include: (a) variation in light intensity, from image to image, during deformation (b) a stochastic pattern that has too fine or too few speckles, (c) analyzing images separated by very small time steps, and (d) very large or very small values of l and δ. Variation in light intensity can cause the stochastic pattern to change in appearance, thereby reducing the ability

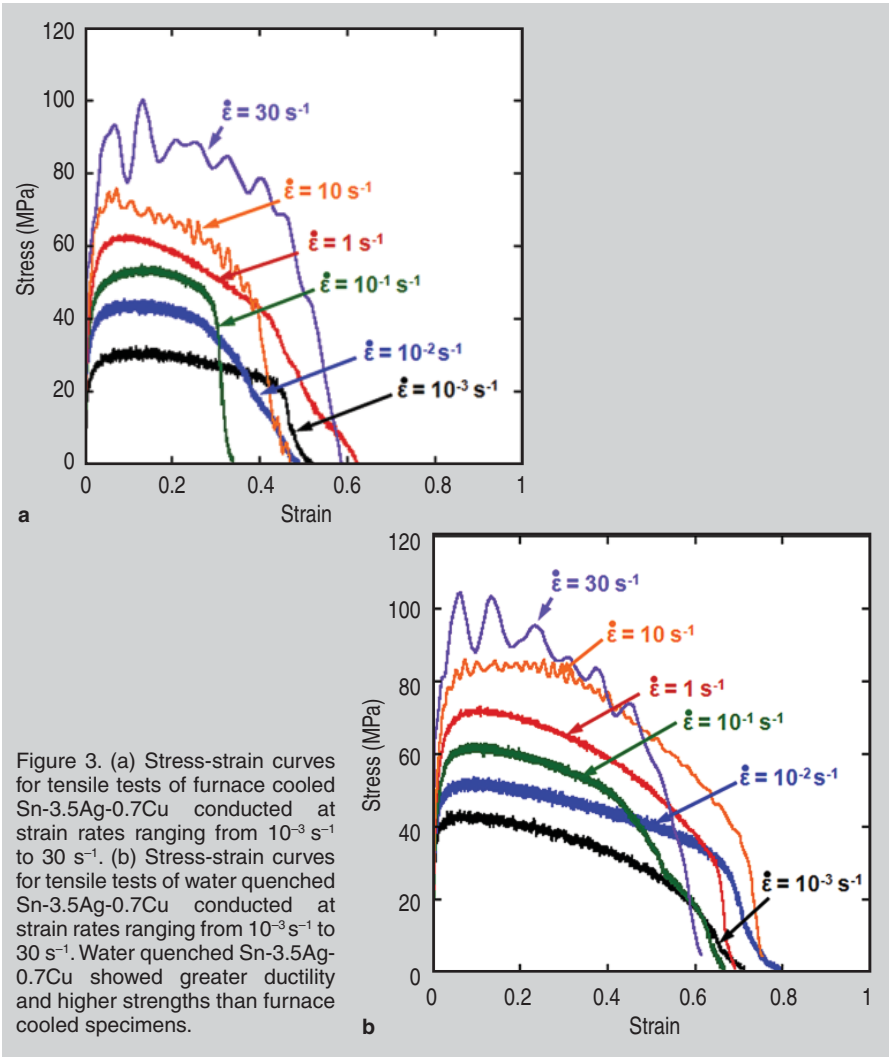

Figure 3. (a) Stress-strain curves for tensile tests of furnace cooled Sn-3.5Ag-0.7Cu conducted at strain rates ranging from 10^{-3} s^{-1} to 30 s^{-1}. (b) Stress-strain curves for tensile tests of water quenched Sn-3.5Ag-0.7Cu conducted at strain rates ranging from 10^{-3} s^{-1} to 30 s^{-1}. Water quenched Sn-3.5Ag-0.7Cu showed greater ductility and higher strengths than furnace cooled specimens.

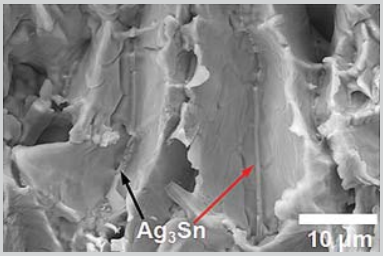

a

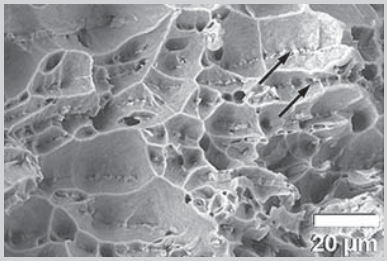

b

Figure 4. Fracture surfaces of furnace cooled Sn-3.5Ag-0.7Cu. (a) Specimen tested at 10^{-3} s^{-1}. Ag_3Sn needles nucleated large voids that decreased ductility. (b) Specimen tested at 30 s^{-1}. Ag_3Sn needles are found at the bottom of ductile dimples. Arrows point to sections of Ag_3Sn needles that fractured.

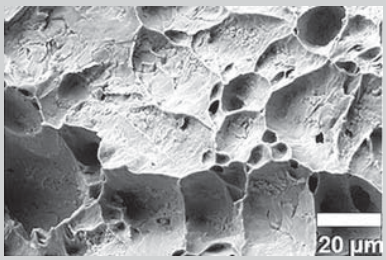

a

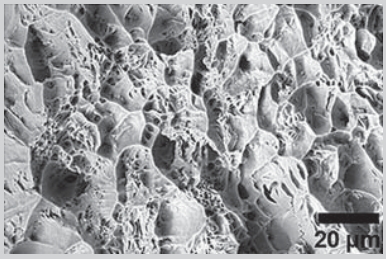

b

Figure 5. Fracture surfaces of water quenched Sn-3.5Ag-0.7Cu. (a) Specimen tested at 10^{-3} s^{-1} showed a relatively smooth surface interspersed with ductile dimples. (b) Fracture surface of test conducted at 30 s^{-1} was rougher due to the higher stresses.

of DIC to track changes in the pattern. A pattern with very fine speckles may be below the resolution of the camera and make correlation difficult. A pattern with too few speckles, or a strain mesh defined with a large δ, does not provide enough points for correlation. Using a small δ effectively creates a fine strain mesh. The fine mesh is more sensitive to light intensity variations and local deformation of the speckles, thereby producing noise. Very large l can also result in too much "averaging" of the displacements. Small time steps correspond to small displacements which may be below the resolution of the system and introduce errors. In order to minimize any artifacts from the variables described above, a parametric study was conducted to determine an optimum time step, l, and δ for our experimental conditions. A test matrix was conducted on images from a tensile test of water quenched Sn-3.5Ag-0.7Cu conducted at a strain rate of 1 s^{-1}. The test matrix encompassed the effects of varying l (ranging between 13–20 pixels) and δ (from 5–15 pixels) on three versions of the tensile test images. The analyses were conducted using different time steps between images, t = 0.001 s, 0.004 s, and 0.017 s.

The effect of changing t, l, and δ was determined by comparing tensile strain and strain rate at the onset of necking, and determining whether the strain and strain rate contours corresponded to the shape and size of the neck in the images. Rigid-body displacement calibrations were also conducted to calibrate the software for actual displacements.

Figure 6 shows the strain and strain rate distribution at necking for l ranging between 13–20 pixels, δ ranging between 5–15 pixels, and t = 0.004 s. The smallest and largest time steps (t = 0.001 s and t = 0.017 s) did not produce strong correlations between strain and strain rate concentrations at the onset of necking. Strain distributions were not particularly sensitive to changes in time step, l, and δ, except for the case of l = 15 pixels and δ = 5 pixels. Using a spacing of δ = 5 pixels effectively created a very fine strain mesh, which was more prone to noise in the strain distribution. Strain rate distributions for all combinations of time step, l, and δ proved to be more sensitive to changes in the variables tested. The smallest time step, t = 0.001 s, corresponded to a displacement between consecutive images that was below the resolution of the DIC software. Thus, these small displacements introduced noise which was readily apparent in the strain rate plots. The combinations of l and δ that exhibited the most variation in strain rate were l = 15 pixels, δ = 5 pixels and l = 20 pixels, δ = 13 pixels. These parameters created facets that overlapped by large amounts. Consequently, those

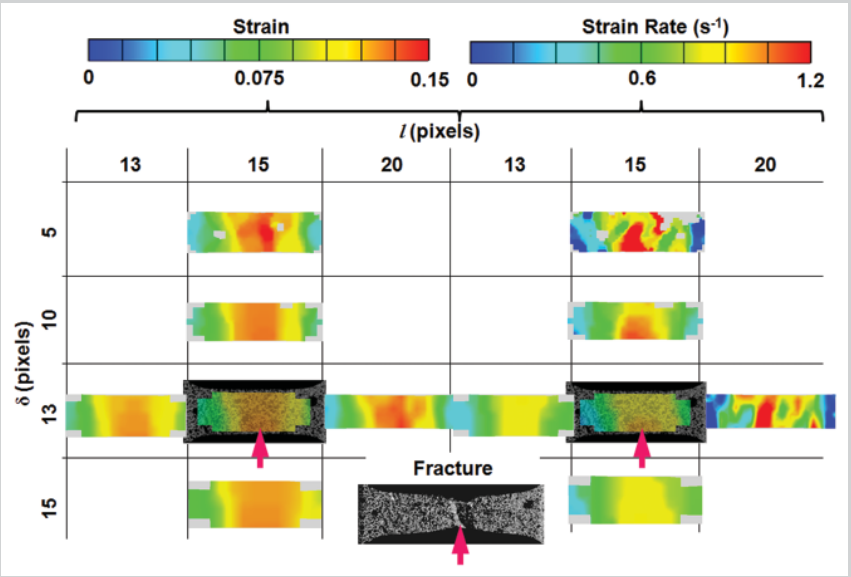

Figure 6. Test matrix comparing the tensile strain and strain rate distribution at necking for l ranging 13–20 pixels, δ ranging 5–15 pixels, and t = 0.004 s. The optimum DIC parameters were t = 0.004 s, l = 15 pixels, and δ = 13 pixels. These parameters represented the experimentally observed necking behavior and fracture location most realistically. The inset image shows the specimen at fracture. Arrows indicate the location of the fracture with respect to the neck.

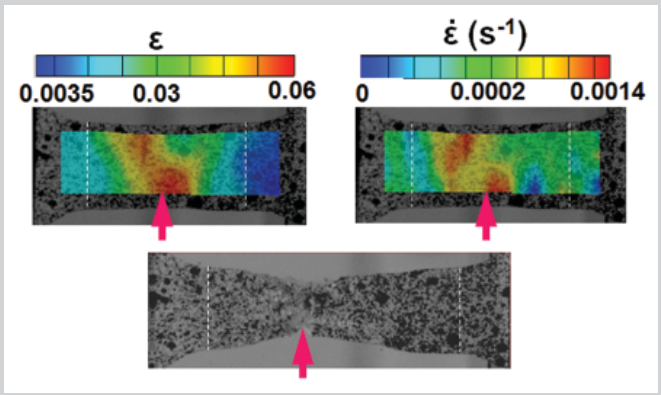

a

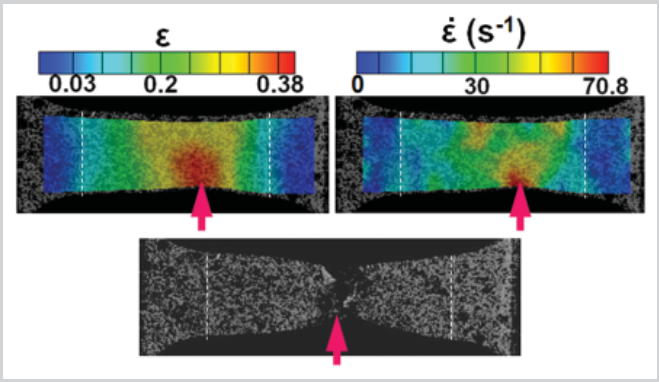

b

Figure 7. (a) Strain and strain rate distributions at necking for a water quenched specimen tested at 10^{-3} s^{-1}. White dotted lines indicated the gage section. A strain concentration is coincident with a strain rate concentration. Arrows indicate the location of fracture and its relation to the strain and strain rate concentrations in the neck. (b) Strain and strain rate distributions at necking for a water quenched specimen tested at 30 s^{-1}.

combinations of l and δ were more sensitive to noise inherent in the high speed video, such as variations in light intensity. The specimen at fracture can be seen as an inset in Figure 6. Arrows indicate the location of fracture with respect to the neck. Figure 6 shows that a time step of 0.004 s, l = 15 pixels and δ = 13 pixels produced strain and strain rate color contour plots that represented the experimentally observed necking behavior and fracture location most realistically. Thus, these settings were used in the DIC analysis to compute strain and strain rate for all the tensile tests.

DIC analysis of the image corresponding to the onset of necking (at ultimate tensile strength) was conducted. Strain and strain rate in the tensile direction were averaged over the neck of the tensile specimen. This region of initial strain intensification corresponded to approximately 1/3 the length of the original gage length for all experiments. As a further check that the neck was correctly located, each DIC analysis was compared to the high speed video, and the neck identified in the image corresponding to the fracture location. Figure 7a and b shows the tensile strain and strain rate contour plots produced for water quenched specimens tested at the lowest strain rate and highest strain rates, respectively. The arrows indicate the location of fracture and its relation to the strain and strain rate concentration in the neck. The average strain as a function of applied strain rate is shown in Figure 8a. The strain in the neck increased with applied strain rate. Water quenched specimens appeared to exhibit larger values of strain in the neck compared to furnace cooled specimens. This may be due to earlier onset of void nucleation and growth in the furnace cooled specimens, as described above. The average strain rate as a function of applied strain rate is shown in Figure 8b. Strain rate in the neck is quite close to the applied strain rate. This is not surprising, since the measurements were taken at the onset of necking. It would be expected that at later stages of necking the local strain rates would increase significantly. We encountered some difficulty in carrying out DIC analysis beyond necking and close to failure of the specimen. The large deformation in the gage section tends to spall the speckle pattern, making it difficult to conduct DIC. Nevertheless, quantification of local strain and local strain rate at the neck was achieved.

CONCLUSIONS

Tensile tests of Sn-3.5Ag-0.7Cu specimens with coarse and fine microstructures were conducted over the strain rate range 10^{-3} s^{-1} – 30 s^{-1}. Strain and strain rate distributions at the onset of necking were analyzed using the digital image correlation. The following conclusions were drawn from the

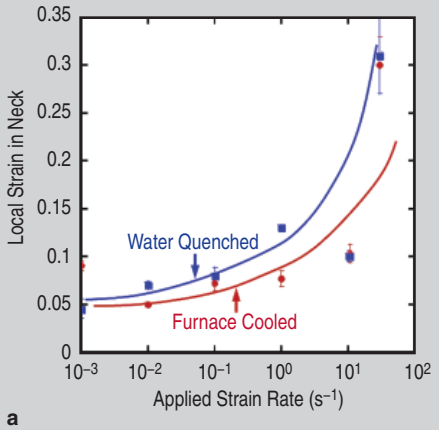

a

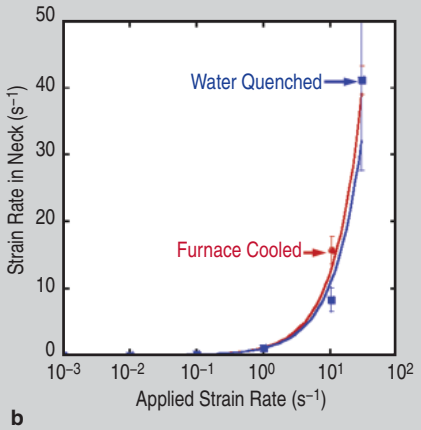

b

Figure 8. (a) Strain in the neck of the tensile specimens at UTS versus applied strain rate. Water quenched specimens reach larger values of strain in the neck compared to furnace cooled specimens. (b) Strain rate in the neck of the tensile specimens at the UTS. The strain rate in the neck is equal to the applied strain rate.

experimental results.

1. Ultimate tensile strength increased with increasing applied strain rate. For a given strain rate, the water quenched specimens had greater UTS values than the furnace cooled specimens.
2. Fractography revealed that the large Ag_3Sn needles in the furnace cooled specimens fractured, nucleated large voids, and resulted in decreased ductility. At the highest strain rate Ag_3Sn needles fractured along their length. The fine eutectic mixture of Ag_3Sn and Cu_6Sn_5 in water quenched specimens nucleated finer voids and resulted in greater ductility. At the highest strain rate the voids became larger.
3. A test matrix was conducted on a tensile test of a speckle coated water quenched specimen to compare the effect of various time steps, l, and δ on the strain and strain rate distributions. The test matrix showed that the optimum DIC parameters for this experimental setup were $t = 0.004$ s, $l = 15$ pixels, and $\delta = 13$ pixels.
4. Tensile strain and strain rate in the neck of the tensile specimens, at the onset of necking, increased with the applied strain rate. Strain in the neck increases with applied strain rate. Strain rate in the neck was nearly equal to the applied strain rate for all tests. There was practically no difference between the strain rates occurring in the neck for both the furnace cooled and water quenched specimens.

ACKNOWLEDGEMENTS

The authors are grateful for the financial support for this work from the National Science Foundation Division of Materials Research–Metals Division (Drs. Alan Ardell, Bruce MacDonald, and Harsh Chopra, Program Directors).The authors gratefully acknowledge the use of facilities within the Center for Solid State Science at Arizona State University.

References

1. N. Chawla, *Int. Mater. Rev.* 54 (6) (2009), pp. 333–367.
2. J. Glazer, *J. Electron. Mater.* 23 (1994), p. 693.
3. J. Glazer, *Int. Mater. Rev.* 40 (2) (1995), pp. 65–93.
4. M. McCormack and S. Jin, *JOM,* 45 (7) (1993), pp. 36–40.
5. P.R. Vianco and D.R. Frear, *JOM,* 45 (7) (1993), pp. 14-18.
6. W.J. Plumbridge, *J. of Mater. Sci.* 3 (1996), p. 2501.
7. R.S. Sidhu and N. Chawla, *Metall. Mater. Trans.* 39A (2008), p. 799.
8. R.S. Sidhu, X. Deng, and N. Chawla, *Metall. Mater. Trans.* 39A (2008), p. 340.
9. M. Kerr and N. Chawla, *Acta Mater.*, 52 (2004), p. 4527.
10. J.E. Field, S.M. Walley, W.G. Proud, H.T. Goldrein, and C.R. Siviour, *Int. J. Impact Eng.,* 30 (2004), p. 725.
11. T.Y. Tee, H.S. Ng, C.T. Lim, E. Pek, and Z. Zhong, *Microelectron. Reliab.,* 44 (2004), p. 1131.
12. D. Reiff and E. Bradley, *Proc. 55th Electronic Components and Technology Conference* (Piscataway, NJ: IEEE, 2005), pp. 1519–1525.
13. M. Date, T. Shoji, M. Fujiyoshi, K. Sato, and K.N. Tu, *54th Electronic Components and Technology Conference* (Piscataway, NJ: IEEE, 2004), pp. 668–674.
14. K.T. Tsai, F.L. Liu, E.H. Wong, and R. Rajoo, *Solder. Surf. Mt. Technol.*, 18 (2) (2006), p. 12.
15. P. Pandher and M. Bourereghda, *IEEE 45th Annual International Reliability Physics Symposium* (Piscataway, NJ: IEEE, 2007), pp. 107–112.
16. K. Newman, *Proc. 55th Electronic Components and Technology Conference* (Piscataway, NJ: IEEE, 2005), pp. 1194–1200.
17. J.Y.H. Chia, B. Cotterell, and T.C. Chai, *Mater. Sci. and Eng. A,* 417 (2006), p. 259.
18. B.L. Boyce and T.B. Crenshaw, "Servohydraulic Methods For Mechanical Testing in the Sub-Hopkinson Rate Regime up to Strain Rates of 500 1/s," Sandia National Laboratory Report SAND2005-5678 (2005).
19. K.E. Yazzie, H. Fei, J.J. Williams, H. Jiang, and N. Chawla, *J. Electron. Mater.,* 38 (2009), p. 2746.
20. *ARAMIS User Manual* (GOM, Braunschweig, Germany, 2005).
21. F. Hild and S. Roux, *Strai,n* 42 (2006), p. 69.
22. M. Sutton, W. Wolters, W. Peters, W. Ranson, and S. McNeill, *Image Vision Comput.,* 1 (1983), p. 133.
23. M.A. Sutton, M. Cheng, W.H. Peters, Y.J. Chao, and S.R. McNeill, *Image Vision Comput.,* 4 (1986), 143.
24. W.N. Sharpe, *Springer Handbook of Experimental Solid Mechanics* (New York: Springer, 2008).
25. M.A. Sutton, J. Orteu, and H. Schreier, *Image Correlation for Shape, Motion and Deformation Measurements* (New York: Springer, 2009).
26. W. An and T.E. Carlsson, *Opt. Laser. Eng.,* 40 (2003), p. 529.
27. I. Yamaguchi, *J. Phys. E: Sci. Instrum.,* 14 (1981), p. 1270.
28. D. Lecompte, A. Smits, S. Bossuyt, H. Sol, J. Vantomme, D. Van Hemelrijck, and A. Habraken, *Opt. Laser Eng.,* 44 (2006), p. 1132.
29. Z. Wang, H. Li, J. Tong, and J. Ruan, *Exper. Mech.,* 47 (2007), p. 701.
30. T. Siebert, T. Becker, K. Spiltthof, I. Neumann, and R. Krupka, *Opt. Eng.,* 46 (2007), p. 051004.
31. J. Orteu, L. Robert, Y. Surrel, P. Vacher, B. Wattrisse, M. Bornert, F. Brémand, P. Doumalin, J. Dupré, M. Fazzini, M. Grédiac, F. Hild, S. Mistou, and J. Molimard, *Exp. Mech.,* 49 (2009), p. 353.
32. B. Wattrisse, A. Chrysochoos, J. Muracciole, and M. Némoz-Gaillard, *Exp. Mech.,* 41 (2001), p. 29.
33. I. Scheider, W. Brocks, and A. Cornec, *J. Eng. Mater.–T ASME*, 126 (2004), p. 70.
34. F. Sánchez-Arévalo, T. García-Fernández, G. Pulos, and M. Villagrán-Muniz, *Mater. Charact.,* 60 (2009), p. 775.
35. F. Sánchez-Arévalo and G. Pulos, *Mater. Charact.,* 59 (2008), p. 1572.
36. P.L. Reu and T.J. Miller, *J. Strain Anal. Eng.,* 43 (2008), p. 673.
37. M. Tschopp, B. Bartha, W. Porter, P. Murray, and S. Fairchild, *Metall. Mater. Trans.,* 40A (2009), p. 2363.
38. H. Jin, W.-Y. Ku, and J. Korellis, *J. Strain Anal. Eng.,* 43 (2008), p. 719.
39. J. Périé, S. Calloch, C. Cluzel, and F. Hild, *Exp. Mech.,* 42 (2002), p. 318.
40. M. Grédiac, *Compos. Part A – Appl S,* 35 (2004), p. 751.
41. D. Zhang and D.D. Arola, *J. Biomed. Opt.,* 9 (2004), p. 691.
42. P. Thurner, B. Erickson, R. Jungmann, Z. Schriock, J. Weaver, G. Fantner, G. Schitter, D. Morse, and P. Hansma, *Eng. Fract. Mech.,* 74 (2007), p. 1928.
43. S. Park, R. Dhakal, L. Lehman, and E. Cotts, *Acta Mater.,* 55 (2007), p. 3253.
44. R.D. Pendse and P. Zhou, *Microelectron. Reliab.,* 42 (2002), p. 301.
45. Yaofeng Sun, J. Pang, Xunqing Shi, and J. Tew, *The Tenth Intersociety Conference on Thermal and Thermomechanical Phenomena in Electronic Systems 2006* (Piscataway, NJ: IEEE, 2006), pp. 921–927.
46. L. Kehoe, V. Guenebaut, and P. Kelly, *Proc. 54th Electronic Components & Technology Conference* (Piscataway, NJ: IEEE, 2004), pp. 120–127.
47. Y. Sun and J.H. Pang, *Microelectron. Reliab.,* 48 (2008), p. 310.
48. P. Lall, D.R. Panchagade, D. Iyengar, S. Shantaram, and H. Schrier, *IEEE Transactions on Components and Packaging Technologies,* 32 (2009), p. 378.
49. X. Shi, H. Pang, X. Zhang, Q. Liu, and M. Ying, *IEEE Transactions on Components and Packaging Technologies,* 27 (2004), p. 659.
50. G. Dieter, *Mechanical Metallurgy* (London: McGraw-Hill Science/Engineering/Math, 1986).
51. P.W. Bridgman, *Studies in Large Plastic Flow and Fracture with Special Emphasis on the Effects of Hydrostatic Pressure* (New York: McGraw-Hill, 1952).

K.E. Yazzie, graduate research assistant, J.J. Williams, assistant research scientist, D. Kingsbury, laboratory manager, P. Peralta, professor, H. Jiang, assistant professor, and N. Chawla, professor, are with the School of Mechanical, Aerospace, Chemical, and Materials Engineering, Fulton Schools of Engineering, Arizona State University, Tempe, AZ 85287-6106. Prof. Chawla can be reached at nchawla@asu.edu.